

emission results for Cs deposition on  $C_{60}$  at 300 K showed that the C 1s core level developed along the general pattern shown in Fig. 1, starting with a sharp main line and  $\pi$ - $\pi^*$  shake-up features, converting to a broad asymmetric feature where the coverage corresponded to a metallic phase, and terminating with a sharp line and the same satellites seen in Fig. 1 when the  $Cs_6C_{60}$  composition was reached. The valence band evolution showed the characteristic growth of a LUMO-derived feature, with broadening and shifting of other filled bands as for K incorporation (5, 6). Despite the larger ionic size of Cs compared to K, facile diffusion was observed and phase separation occurred at 300 K for thin films.

Figure 2 shows the valence band emission from a 12-layer-thick  $Cs_6C_{60}$  film grown by saturated Cs exposure and annealing to 475 K to remove any excess surface Cs and to improve crystallinity. These results are analogous to those of Benning *et al.* (5) and the C 1s lineshape is the same as that for  $K_6C_{60}$ . The addition of six layers of  $C_{60}$  at 300 K resulted in a reduction of the LUMO emission, consistent with Cs redistribution through the 18-layer film with  $x = 4$  nominal stoichiometry. The spontaneous outdiffusion of Cs demonstrates that the  $Cs_6C_{60}$  layer was unstable in the presence of  $C_{60}$ . The broadening in valence band emission, evident by the filling-in of the valley between peaks 2 and 3, can be attributed to overlapping contributions from intimately mixed insulating and metallic phases. The third curve in Fig. 2 shows the valence band emission after addition of seven more layers of  $C_{60}$  for a total film thickness of 25 monolayers. In this case, the LUMO-derived band is much weaker than expected for a nominal  $Cs_{2.8}C_{60}$  film. This could be explained by formation of a stable  $Cs_3C_{60}$  phase, followed by the formation of a  $C_{60}$  overlayer free of Cs. This  $C_{60}$  layer would attenuate the emission from the metallic phase and contribute intensity at the positions indicated by vertical tic marks in Fig. 2. This scenario would also explain the filling-in of the valley between peaks 2 and 3 and the broadening of peak 3 for the mixed phase. We conclude that a metallic phase forms at the expense of  $Cs_6C_{60}$  at the  $C_{60}$ - $Cs_6C_{60}$  heterojunction and that this phase is then stable when in contact with  $C_{60}$ .

Previous photoemission studies of  $K_xC_{60}$  emphasized changes in the valence bands, correctly noting the filling of the LUMO-derived bands (5, 6). Here, we have shown that the films produced are two-phase with distinct separation between  $C_{60}$  and the  $K_3C_{60}$  phases. For growth at 300 K, thermodynamics dictate phase separation, but the details of nucleation and growth pro-

duce fine mixtures. Annealing to promote grain growth should produce higher quality samples as desired for superconductivity and electrical characterization. The present results demonstrate that the  $C_{60}$ - $K_3C_{60}$  heterojunction is stable and that an analogous structure exists for the  $Cs_xC_{60}$  system.  $C_{60}$  boundaries with  $K_6C_{60}$  or  $Cs_6C_{60}$  are not stable. This suggests that insulating-superconducting heterostructures can be fabricated. Such devices are presently under investigation.

#### REFERENCES AND NOTES

1. R. C. Haddon *et al.*, *Nature* **350**, 320 (1991).
2. A. F. Hebard *et al.*, *ibid.*, p. 600.
3. K. Holczer *et al.*, *Science* **252**, 1154 (1991).
4. M. J. Rosseinsky *et al.*, *Phys. Rev. Lett.* **66**, 2830 (1991).
5. P. J. Benning, J. L. Martins, J. H. Weaver, L. P. F.

6. G. K. Wertheim *et al.*, *ibid.*, p. 1419.
7. O. Zhou *et al.*, *Nature* **351**, 462 (1991).
8. P. W. Stephens *et al.*, *ibid.*, p. 632.
9. J. L. Martins, N. Troullier, M. C. Schabel, in preparation.
10. Y. Z. Li *et al.*, *Science* **253**, 429 (1991).
11. S. Saito and A. Oshiyama, in preparation.
12. R. E. Haufler *et al.*, *J. Phys. Chem.* **94**, 8634 (1990).
13. Unpublished results involving sample preparation and characterization based on photoemission and inverse photoemission for Na, K, and Cs in  $C_{60}$  and  $C_{70}$  films.
14. J. H. Weaver *et al.*, *Phys. Rev. Lett.* **66**, 1741 (1991).
15. M. B. Jost *et al.*, *Phys. Rev. B*, in press.
16. This work was supported by the Office of Naval Research, the National Science Foundation, and the Robert A. Welch Foundation. The synchrotron radiation experiments were done at Aladdin, a facility operated by the University of Wisconsin for the National Science Foundation.

24 June 1991; accepted 10 July 1991

## Interior Structure of Neptune: Comparison with Uranus

W. B. HUBBARD, W. J. NELLIS, A. C. MITCHELL, N. C. HOLMES, S. S. LIMAYE, P. C. MCCANDLESS

**Measurements of rotation rates and gravitational harmonics of Neptune made with the Voyager 2 spacecraft allow tighter constraints on models of the planet's interior. Shock measurements of material that may match the composition of Neptune, the so-called planetary "ice," have been carried out to pressures exceeding 200 gigapascals (2 megabars). Comparison of shock data with inferred pressure-density profiles for both Uranus and Neptune shows substantial similarity through most of the mass of both planets. Analysis of the effect of Neptune's strong differential rotation on its gravitational harmonics indicates that differential rotation involves only the outermost few percent of Neptune's mass.**

PRIOR TO THE 1989 ENCOUNTER OF the Voyager 2 spacecraft with Neptune, there were only crude constraints on the possible composition and structure of Neptune, and considerable controversy existed about whether Uranus and Neptune's similarity in size and mass extended to their deep interiors. Basic constraints on the interior structure of a rotating liquid planet such as Uranus or Neptune are derived from knowledge of the mass  $M$  and equatorial radius at 1-bar pressure  $a$ , and the dimensionless zonal gravitational multipole moments  $J_2, J_4$  of the external gravitational potential which arise in response to the planet's rotation (1-4), all of which were measured during the 1989 encounter. In

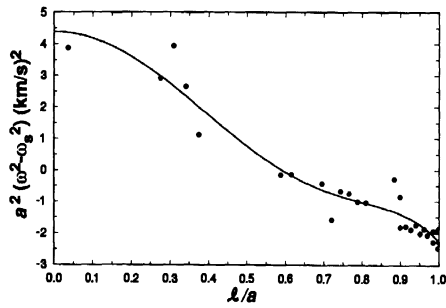
this report we focus on inferences about the composition of the deep interiors of Uranus and Neptune which are obtained by comparing admissible pressure-density relations with shock-compression measurements of likely constituent material (5-7). We also address the problem of how the interior structure responds to the strong differential rotation which was observed in Voyager 2 images.

Table 1 summarizes our knowledge of the Neptunian interior resulting from the Voyager 2 flyby. The rotation period of the magnetic field (3),  $P_S$ , is taken to be the solid-body interior rotation period of Neptune. This parameter enters into the calculation of the dimensionless quantity  $q = \omega_S^2 a^3/GM$ , which characterizes the magnitude of the planet's rotational distortion ( $\omega_S = 2\pi/P_S$  and  $G$  is the gravitational constant). According to the theory of the hydrostatic response of a planet to rotation (8), the dimensionless mass quadrupole moment  $J_2$  (normalized to radius  $a$ ) is to first order

W. B. Hubbard, Lunar and Planetary Laboratory, University of Arizona, Tucson, AZ 85721.  
W. J. Nellis, A. C. Mitchell, N. C. Holmes, P. C. McCandless, University of California, Lawrence Livermore National Laboratory, Livermore, CA 94550.  
S. S. Limaye, Space Science and Engineering Center, University of Wisconsin-Madison, 1225 West Dayton Street, Madison, WI 53706.

**Table 1.** Parameters constraining interior structure.

	Neptune	Uranus
$M$ (earth masses)	17.14	14.53
$a$ (km)	$24764 \pm 20$	$25559 \pm 4$
$P_S$ (hours)	$16.11 \pm 0.05$	$17.24 \pm 0.01$
$q$	$0.0261 \pm 0.0002$	$0.02951 \pm 0.00005$
$J_2(a) \times 10^6$	$3538 \pm 9$	$3516 \pm 3$
$\Lambda_2 = J_2/q$	$0.136 \pm 0.0018$	$0.1191 \pm 0.0003$
$J_4(a) \times 10^6$	$-38 \pm 10$	$-31.9 \pm 5$
$\Lambda_4 = -J_4/q^2$	$0.056 (+0.027, -0.016)$	$0.037 \pm 0.006$
$\langle \rho \rangle$ (g/cm <sup>3</sup> )	1.64	1.27
$C/Ma^2$	0.24	0.23



**Fig. 1.** Differential rotation in Neptune's atmosphere. Points show data from Limaye *et al.* (9); solid curve is a least-squares fit of Eq. 3.

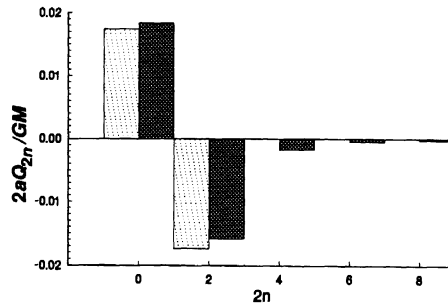


**Fig. 2.** Dimensionless harmonic components of solid-body rotational potential (light bars) and of rotational potential for the law of Fig. 1 (darker bars).

proportional to  $q$ , and the proportionality constant  $\Lambda_2$  constrains the interior mass distribution in the sense that the smaller  $\Lambda_2$ , the more centrally condensed is the planet. The Radau-Darwin approximation (8) provides a unique and monotonic relationship between  $\Lambda_2$  and the axial moment of inertia  $C$ , but is not highly accurate for planets as centrally condensed as Uranus and Neptune. Thus the dimensionless moment of inertia  $C/Ma^2$  given in Table 1 is slightly model-dependent, but is basically derived from  $\Lambda_2$ , with the similar values of  $C/Ma^2$  for Neptune and Uranus reflecting similar values for  $\Lambda_2$ . As we show below, the higher value of Neptune's mean density  $\langle \rho \rangle$  as compared with Uranus' mainly reflects greater self-compression rather than a major difference in composition.

For solid-body rotation, the centrifugal potential in the planet's frame is given by

$$Q_S = \frac{1}{2} \omega_S^2 l^2 \quad (1)$$

where  $l$  is the distance from the rotation axis. If we resolve  $Q_S$  into spherical harmonic components, it has only zonal components of degree zero and degree two, with the latter component directly exciting  $J_2$ . Since there is no degree four component in  $Q_S$ ,  $J_4$  is indirectly excited by components of order  $Q^2$  (that is, of order  $q^2$ ), and is invariably of opposite sign to  $J_2$ . In this case the mass

distribution in the planet is further constrained by  $J_4 = -\Lambda_4 q^2$ , again in the sense that the smaller  $\Lambda_4$ , the smaller the fraction of mass in the planet's outermost layers.

Measurements of cloud motions in Voyager 2 images show that Neptune has a wide equatorial zone which rotates more slowly than the magnetic field, with a period of about 18 hours, while regions near the pole rotate more rapidly than the magnetic field (9, 10). The differential rotation is more pronounced than in any other object in the solar system and would involve significant mass if it were deeply rooted. Suomi *et al.* (11) have shown that the cloudtop winds in low latitudes could originate as deep as 2000 to 3000 km ( $l/a \sim 0.9$ ) if the deeper atmosphere rotates at rate  $\omega_S$ . As a limiting case, we consider rotation on concentric cylinders, that is,  $\omega = \omega(l)$ . In this case, in place of Eq. 1, the centrifugal potential  $Q$  experienced by an element of fluid at distance  $l$  from the rotation axis is given by  $Q = Q_S + \Delta Q$ , where (12)

$$\Delta Q = \int_0^l l' dl' [\omega(l')^2 - \omega_S^2] \quad (2)$$

Thus if we fit to the observed cloud motions a function of the form

$$a^2[\omega(l)^2 - \omega_S^2] = 2A_2 + 4A_4(l/a)^2 + 6A_6(l/a)^4 + 8A_8(l/a)^6 \quad (3)$$

with  $A_2, A_4, \dots$  as free parameters,  $\Delta Q$  can be calculated and used to calculate the equilibrium planetary structure and resulting gravitational moments. Figure 1 shows the least-squares fit of Eq. 3 to cloud motion data from Voyager 2 measurements. The distribution of angular momentum per unit mass which is inferred from Eq. 3 increases monotonically with  $l$ . It does not violate the Solberg stability criterion (13) and thus cannot be ruled out a priori.

Differential rotation can have a substantial effect on the higher gravitational zonal harmonics of Neptune. Figure 2 shows the harmonic components  $Q_{2n}$  of  $Q$  evaluated on a sphere of radius  $a$ , compared with the harmonic components of  $Q_S$ . For the rotation law shown in Fig. 1, the components  $2n = 2, 4, 6, 8$  all have the same sign instead of alternating in sign, and the component  $Q_4$  substantially exceeds  $Q_2^2$ . If the mass of the differentially rotating portions of Neptune were significant, one would expect Neptune's gravitational harmonics  $J_2$  and  $J_4$  to have the same rather than opposite sign.

Interior profiles of pressure  $P$  and mass density  $\rho$  as a function of mean radius  $r$  are calculated by fitting to the constraints of Table 1 using the method of Hubbard and Marley (14). Both Uranus and Neptune are assumed to have a central rocky core with chondritic bulk proportions of iron, oxygen, magnesium, and silicon, and an intermediate envelope composed of "ice," with "ice" defined as a mixture of the molecules  $H_2O$ ,  $CH_4$ , and  $NH_3$  in solar proportions, not necessarily with intact molecules, and almost certainly in a liquid phase because of elevated temperatures. Observations of the atmospheric composition of both planets show predominantly hydrogen atmospheres, with a solar proportion of helium in the case of Uranus, and with substantial enrichment of carbon (C/H is about 30 times solar in both atmospheres) (15). Thus the outermost layer is taken to have a pressure-density relation appropriate to solar composition (denoted in this paper with the symbol  $\odot$ ), or to solar composition with a small density enhancement, and at constant specific entropy with the entropy fixed to the value near 1-bar pressure, at a temperature of 70 K (2).

Figure 3 shows three possible  $\rho(r)$  profiles for Neptune, as well as a previously published model for Uranus (dotted curve) (14). Two of the Neptune models (N1 and N3) have small rocky cores together with extensive outer envelopes composed of "ice" at temperatures from  $\sim 3000$  K at pressures of about 0.3 Mbar to  $\sim 7000$  K near the center at 6 Mbar. These models have a gradual transition from "ice" to a hydrogen-

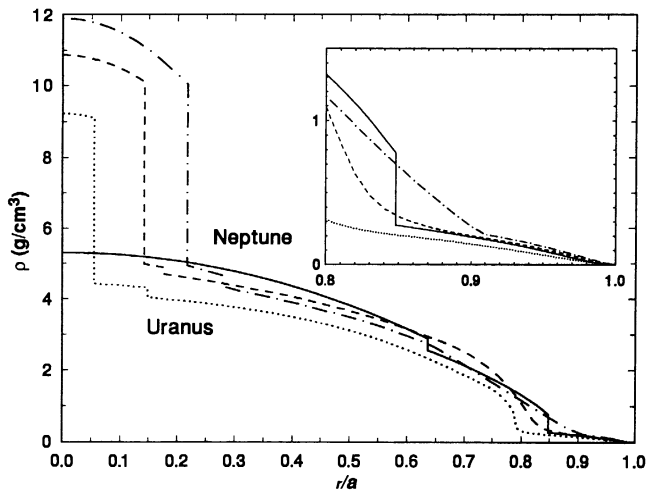


**Fig. 3.** Neptune models N1 (dash-dot curve), N2 (solid curve), and N3 (dashed curve), compared with a Uranus model. Model N2d would be indistinguishable from N2 on this plot. Inset shows the region of transition to a hydrogen-rich atmosphere in more detail.

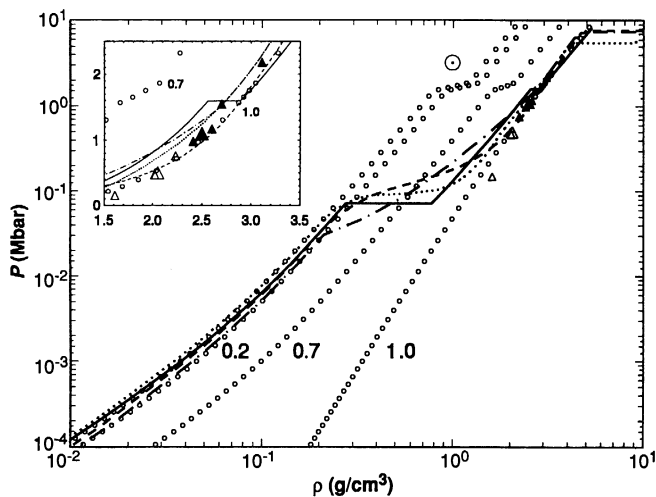


**Fig. 4.** Pressure versus density profiles in Neptune and Uranus, coded as in Fig. 3, compared with adiabats for various mixtures of solar composition and “ice,” and with single-shock (open triangles) and double-shock (filled triangles) data points for “synthetic Uranus.” Larger triangles show shock points for which temperature was measured. Inset shows comparison of models and shock data in more detail, on a linear scale in both coordinates.

rich atmosphere at pressures  $\sim 0.1$  Mbar. An equally acceptable interior model of Neptune (N2) has, instead of a rock core, a large central zone of cold “ice” mixed with 15% rock by mass, together with an outer envelope of pure “ice.” All of these models (N1, N2, N3) assume solid-body rotation with period  $P_s$  and match the observed values of  $M$ ,  $a$ , and  $J_2$ . Their values of  $J_4 \times 10^6$  ( $-34.5$ ,  $-31.4$ , and  $-31.9$ , respectively) are also compatible with the observed value in Table 1.

To determine whether assumed rotation on cylinders significantly affects the models, we computed model N2d, which obeys the differential rotation law shown in Eq. 3 and Fig. 1. This model also matches the observed values of  $M$ ,  $a$ , and  $J_2$ , and the run of density and pressure with radius differs only slightly from model N2. However, model N2d must be discarded because its value of  $J_4 \times 10^6$  is  $+72.1$ , which falls well outside the observed range (Table 1).

To determine whether the density enhancement of Neptune models with respect to Uranus models is due to self-compression

or to compositional differences, we plot the models in Fig. 4 on the pressure-density plane. In this figure, the curves marked with open circles show various constant-entropy curves for pure solar composition (uppermost curve marked with  $\odot$ ), and for mixtures of solar composition with the specified ice mass fraction, ending with pure “ice” (lowest curve). Other lines show the Uranus models and the three Neptune models, denoted as in Fig. 3.

High pressures, densities, and temperatures in the giant planets can be obtained in the laboratory by shock compression of liquids (16). For this reason we have studied a liquid mixture called “synthetic Uranus” at high shock pressures achieved with a two-stage gas gun. This mixture is H-rich with molar abundances of H, O, C, and N approximately equal to those of planetary “ice.” The liquid is a solution of water, ammonia, and isopropanol with mole fractions of 0.71, 0.14, and 0.15, respectively. Single-shock equation of state (EOS), electrical conductivity, and temperature data were measured previously (6, 7) for “syn-

thetic Uranus” up to 0.7 Mbar. We add here new double-shock EOS data up to 2.2 Mbar. All of the shock data are plotted as triangles in Fig. 4. The single-shock point at 0.499 Mbar and the double-shock point at 1.10 Mbar also had temperatures independently measured at  $3220 \pm 200$  K and  $4100 \pm 300$  K respectively; these numbers are similar to the values calculated at these pressures on planetary adiabats in Neptune and Uranus, so that the effect of uncertainty in the thermal pressure on the comparison should be minimal.

Within the nonuniqueness of present interior models, Uranus and Neptune obey virtually the same pressure-density law, and both resemble and might be composed of pure “ice” at pressures greater than about 1 Mbar. The rock core mass in all of our models of Uranus and Neptune is so small that it could well be zero. These results are consistent with initial Uranus and Neptune interior models based on the new Voyager 2 data (17). Thus we have the problem of accounting for the expected mass fraction of rock in a condensate of solar composition. For a condensate of iron and magnesium silicates (rock) and “ice” in chemical equilibrium at the low temperatures where Uranus and Neptune formed, we expect a mass ratio of about 1/2.7 for rock/“ice.” For nonequilibrium nebular models with carbon bound up in CO (18), the ratio approaches unity, increasing the problem of accounting for the rock in Neptune models.

The value of Uranus’  $J_2$  and  $J_4$  have been determined with considerable precision from extended observations of the motions of eccentric rings (19), but comparable data are not yet available for Neptune. Although Neptune also possesses rings, only three dense azimuthally confined arcs can be reliably detected from ground-based stellar occultation observations (1, 20). If the Neptunian arcs prove to be on eccentric or inclined orbits, eventually it may be possible to amass enough data to constrain the Neptunian gravity potential to precision comparable to the Uranus measurements. In the meantime, the gravity data from Voyager 2 are sufficient to show that Neptune’s atmospheric differential rotation does not map onto cylinders extending through the interior. The assumption of rigid rotation adopted by Suomi *et al.* (11) for explaining the rapid retrograde winds appears to be valid. Nevertheless, if enough mass is involved in the winds to reduce  $J_4$  significantly in absolute value, caution is in order in interpreting the observed value of  $J_4$  for both Neptune and Uranus.

In our view, the resemblance of the interior pressure-density profile to that of pure

“ice” may be to some extent coincidental. It is possible that material in the deep interior contains both a component which is lighter than “ice,” perhaps hydrogen and helium, and one which is heavier, that is, rock, and is more or less uniformly mixed. Fixing the interior rock/“ice” ratio to the solar value, we find for Uranus and Neptune that the total mass fraction of free hydrogen and helium is about 0.14 in both planets, with about one-third to one-fifth of this component (that is, about 0.05 in N1 and N3, and about 0.03 in N2) in the outermost atmospheric region at pressures smaller than 100 kbar, and the remainder distributed uniformly through the interior.

With such a small total mass fraction of hydrogen and helium, the deuterium to hydrogen number ratio (D/H) in the atmospheres of Uranus and Neptune should be about the same, and equal to the elevated value for primordial ices in other water-rich solar system bodies, that is, about  $2 \times 10^{-4}$ , rather than equal to the primordial nebular value of about  $2 \times 10^{-5}$  which is seen in the atmospheres of Jupiter and Saturn (21). Recent observations of deuterium in the atmospheres of Uranus and Neptune have confirmed that this is the case (22).

One of the most striking differences between Uranus and Neptune is the substantial net interior heat flow for Neptune. The heat flow for Uranus is so far undetectable and significantly smaller than the value for Neptune (23). Attempts to model this difference have taken the path of either relating it to differences in interior structure, with the possibility of pronounced chemical gradients suppressing heat flow in Uranus (24), or to relating it to atmospheric effects which may suppress convection in Uranus due to its greater proximity to the sun (17, 25, 26). The similarity of interior structure which we infer here, and which had been suggested in earlier models (27), makes the second explanation more attractive.

#### REFERENCES AND NOTES

1. B. A. Smith *et al.*, *Science* **246**, 1422 (1989).
2. G. L. Tyler *et al.*, *ibid.*, p. 1466.
3. J. W. Warwick *et al.*, *ibid.*, p. 1498.
4. W. M. Owen, Jr., R. M. Vaughn, S. P. Synnott, *Astron. J.* **101**, 1511 (1991).
5. A. C. Mitchell and W. J. Nellis, *J. Chem. Phys.* **76**, 6273 (1982).
6. W. J. Nellis *et al.*, *Science* **240**, 779 (1988).
7. H. B. Radousky, A. C. Mitchell, W. J. Nellis, *J. Chem. Phys.* **93**, 8235 (1990).
8. V. N. Zharkov and V. P. Trubitsyn, *Physics of Planetary Interiors* (Pachart, Tucson, AZ, 1978); W. B. Hubbard, *Planetary Interiors* (Van Nostrand Reinhold, New York, 1984).
9. S. S. Limaye, L. A. Stromovsky, V. E. Suomi, *Adv. Space Res.*, in press.
10. S. S. Limaye and L. A. Stromovsky, *J. Geophys. Res.*, in press.
11. V. E. Suomi, S. S. Limaye, D. R. Johnson, *Science* **251**, 929 (1991).
12. W. B. Hubbard, *Icarus* **52**, 509 (1982).

13. J.-L. Tassoul, *Theory of Rotating Stars* (Princeton Univ. Press, Princeton, NJ, 1978), p. 167.
14. W. B. Hubbard and M. S. Marley, *Icarus* **78**, 102 (1989).
15. D. Gautier and T. Owen, in *Origin and Evolution of Planetary and Satellite Atmospheres*, S. K. Atreya, J. B. Pollack, M. S. Matthews, Eds. (Univ. of Arizona Press, Tucson, 1989), pp. 487–512.
16. M. Ross, in *High Pressure in Research and Industry*, C. M. Backman, T. Johannisson, L. Tegner, Eds. (Arkittektkopia, Uppsala, 1982), vol. 2, pp. 721–727.
17. M. Podolak, R. T. Reynolds, R. Young, *Geophys. Res. Lett.* **17**, 1737 (1990).
18. R. G. Prinn and B. Fegley, *Astrophys. J.* **249**, 308 (1981).
19. R. G. French *et al.*, *Icarus* **73**, 349 (1988).
20. W. B. Hubbard *et al.*, *Nature* **319**, 636 (1986).
21. W. B. Hubbard and J. J. MacFarlane, *Icarus* **44**, 676 (1980).
22. C. de Bergh, B. L. Lutz, T. Owen, J.-P. Maillard,

- Astrophys. J.* **355**, 661 (1990).
23. J. C. Pearl *et al.*, *Icarus* **84**, 12 (1990).
24. M. Podolak, W. B. Hubbard, D. J. Stevenson, in *Uranus*, J. T. Bergstrahl, E. D. Miner, M. S. Matthews, Eds. (Univ. of Arizona Press, Tucson, in press).
25. W. B. Hubbard and J. J. MacFarlane, *J. Geophys. Res.* **85**, 225 (1980).
26. A. P. Ingersoll and C. C. Porco, *Icarus* **35**, 27 (1978).
27. M. Podolak, R. Young, R. T. Reynolds, *ibid.* **63**, 266 (1985).
28. Work at the University of Arizona was supported by NASA grant NAGW-1555. Work at Lawrence Livermore National Laboratory was performed under the auspices of the U.S. Department of Energy under contract W-7405-ENG-48, with partial support from NASA under contract W-16.180. The “synthetic Uranus” was provided by M. Nicol of UCLA.

1 May 1991; accepted 5 July 1991

## Relations Among Fault Behavior, Subsurface Geology, and Three-Dimensional Velocity Models

ANDREW J. MICHAEL AND DONNA EBERHART-PHILLIPS

The development of three-dimensional P-wave velocity models for the regions surrounding five large earthquakes in California has led to the recognition of relations among fault behavior and the material properties of the rocks that contact the fault at seismogenic depths; regions of high moment release appear to correlate with high seismic velocities whereas rupture initiation or termination may be associated with lower seismic velocities. These relations point toward a physical understanding of why faults are divided into segments that can fail independently, an understanding that could improve our ability to predict earthquakes and strong ground motion.

FAULTS EXHIBIT BEHAVIORS RANGING from aseismic creep to brittle rupture in great earthquakes. Along the length of one fault, these variations can divide the fault into segments that fail independently (1). To investigate the mechanism controlling these variations, we have determined three-dimensional (3-D) P-wave velocity ( $V_p$ ) models for the regions surrounding five moderate-to-large earthquakes in California. The 3-D  $V_p$  models, derived from local earthquake arrival-time data, provide indications of variations in the subsurface geology at seismogenic depths that may relate to the slip behavior of the faults. The five mainshocks studied (Fig. 1) are the magnitude  $M = 6$  1966 Parkfield earthquake, the  $M = 6.7$  1983 Coalinga earthquake (2), the  $M = 6.1$  1985 Kettleman Hills earthquake (2), the  $M = 6.2$  1984 Morgan Hill earthquake (3), and the  $M = 7.1$  1989 Loma Prieta earthquake (4).

We calculated the 3-D  $V_p$  models using simultaneous inversion of local arrival-time data for the velocity model and the locations of the seismic sources. The arrival time of a seismic wave at a seismographic station de-

pends on the time at which the wave originated (origin time), the location from which the wave originated (hypocenter), the location of the station, and the seismic velocities of the rocks along the raypath from the source to the station. The hypocenter, and sometimes the origin time, are known for explosions, whereas neither is known for earthquakes. The inversion process starts with initial estimates of the velocity model,

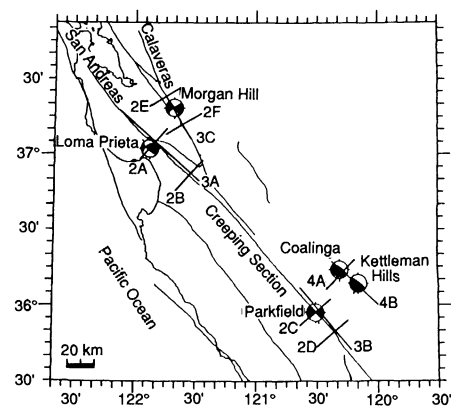


Fig. 1. Map of the five mainshocks studied showing their focal mechanisms, the locations of the cross sections shown in Figs. 2, 3, and 4 and the San Andreas and Calaveras faults.

Branch of Seismology, Mail Stop 977, U.S. Geological Survey, 345 Middlefield Road, Menlo Park, CA 94025.